

## Article

# Research on Mechanical Properties of a 3D Concrete Printing Component-Optimized Path by Multimodal Analysis

Bolin Wang<sup>1,2</sup>, Min Yang<sup>2</sup>, Shilong Liu<sup>2</sup>, Xianda Liu<sup>3</sup>, Hongyu Zhao<sup>4,5,\*</sup>, Xiangyu Wang<sup>3</sup>, Yishuang Liang<sup>2</sup> and Xiaofei Yao<sup>2,\*</sup>

<sup>1</sup> School of highway, Chang'an University, Xi'an 710064, China; wbl1993lang@163.com

<sup>2</sup> CCCC First Highway Consultants Co., Ltd., Xi'an 710075, China; yangmincccc@sina.com (M.Y.); sl19941207@gmail.com (S.L.); yishuang.liang@outlook.com (Y.L.)

<sup>3</sup> School of Civil Engineering and Architecture, East China Jiao Tong University, Nanchang 330013, China; 18879671461@163.com (X.L.); xiangyu.wang@curtin.edu.au (X.W.)

<sup>4</sup> School of Civil Engineering, Chongqing University, Chongqing 400045, China

<sup>5</sup> Institute for Smart City of Chongqing University in Liyang, Chongqing University, Liyang 213300, China

\* Correspondence: 20211601069@cqu.edu.cn (H.Z.); 235134742@163.com (X.Y.)

**Abstract:** Three-dimensional concrete printing (3DCP) technology with solid wastes has significant potential for sustainable construction. However, the hardened mechanical properties of components manufactured using 3DCP technology are affected by weak interlayer interfaces, limiting the widespread application of 3DCP technology. To address the inherent limitations of 3DCP technology, conventional improvement strategies, such as external reinforcement and the optimization of material properties, lead to increased production costs, complex fabrication, and decreased automation. This study proposes an innovative spatial path optimization method to enhance the mechanical performance of 3D-printed, cement-based components. The novel S-path design introduces additional printed layers in the weak interlayer regions of the printed samples. This design improves the spatial distribution of fiber-reinforced filaments in continuous weak zones, thus enhancing the functional efficiency of fibers. This approach improves the mechanical performance of the printed samples, achieving compressive strengths close to those of cast samples and only a 20% reduction in average flexural strength. Compared to using a conventional printing path, the average compressive strength and flexural strength are improved by 30% and 55%, respectively, when the S-path layout is employed in 3DCP. Additionally, this method significantly reduces the anisotropy in compressive and flexural strengths to 26% and 28% of samples using conventional printing paths, respectively. Therefore, the proposed method can improve the mechanical properties and stability of the material, reducing the safety risks of printed structures.

**Keywords:** 3D concrete printing; path optimization; fiber reinforcement; anisotropy; solid wastes



**Citation:** Wang, B.; Yang, M.; Liu, S.; Liu, X.; Zhao, H.; Wang, X.; Liang, Y.; Yao, X. Research on Mechanical Properties of a 3D Concrete Printing Component-Optimized Path by Multimodal Analysis. *Sustainability* **2024**, *16*, 9388. <https://doi.org/10.3390/su16219388>

Academic Editor: Shengwen Tang

Received: 25 July 2024

Revised: 28 September 2024

Accepted: 11 October 2024

Published: 29 October 2024



**Copyright:** © 2024 by the authors. Licensee MDPI, Basel, Switzerland. This article is an open access article distributed under the terms and conditions of the Creative Commons Attribution (CC BY) license (<https://creativecommons.org/licenses/by/4.0/>).

## 1. Introduction

The carbon emissions of the construction industry account for nearly 40% of global energy-related carbon emissions [1]. Therefore, the United Nations Framework Convention on Climate Change (COP27) emphasizes the significance of adopting new technologies to achieve sustainability in construction [2]. Digital fabrication, or 3DCP (3D concrete printing) technology, is offered to resolve present challenges by introducing enhanced construction automation, design flexibility, production green sustainability, cost saving, and removing the use of framework [3,4]. The design flexibility of 3DCP enables the optimization of material distribution and the minimization of unnecessary material usage [5–7]. Removing the framework contributes to a reduction in tree consumption and carbon emissions. Moreover, the utilization of industrial waste, such as fly ash (FA) and silica fume (SF), to replace cement or aggregates in 3DCP reduces carbon emissions and promotes waste recycling [8]. Consequently, 3DCP technology with solid wastes significantly enhances

sustainability by optimizing material use, reducing framework use, and reducing cement, thereby lowering carbon emissions. The application of 3DCP in practical engineering fields, such as prefabricated structural components, building construction, and bridge infrastructure, has been rapidly developed due to these advantages [9–11].

Construction using 3DCP technology is a process in which the nozzle of the printer moves and continuously extrudes cementitious material along a pre-set path, thus requiring a distinctive selection of raw materials and a mixed design compared to traditional concrete [12,13]. To ensure the success of 3DCP, process-related material characteristics, such as pumpable, extrudable, buildable, and mechanical performance, have attracted more and more attention all over the world [14,15]. However, the procedure of depositing layer-by-layer leads to weak interfaces between horizontally connected layers, which generates potential defects in the same orientation of printed components [16,17]. Meanwhile, inconsistent deformation and the discontinuous mechanical properties of the structure generated by these defects can induce continuous structural damage due to the concentration of stresses, weakening the overall load-bearing capacity and long-term durability of the structure [18,19].

The bond strength of interlayer weak areas significantly influences the quality of the printed structure [20,21]. For the samples printed using the conventional path, fibers are incorporated to enhance the mechanical properties. Nevertheless, this phenomenon of weak areas between layers is accentuated as the fiber content increases [22,23]. Sanjayan et al. [24] discovered that the water content between interlayers is determined by various parameters, such as the printing process, evaporation rate, water permeability of the mixture, and the water discharged to the surface during the extrusion process, therefore obviously influencing the interlayer bonding strength [25,26]. To reinforce weak interfaces by accelerating the strength development of printed structures, some external reinforcement methods have been applied. Van et al. [27] and Marchment et al. [28] explored the impact of surface roughness and print-time intervals on the interlayer strength of extrusion-based 3D-printed concrete, finding that the mechanical performance of the weaker middle areas between filaments was significantly influenced by the printing parameters. Hence, identifying effective strategies to boost and guarantee the interlayer bond strength within 3D-printed concrete structures is key to enhance their overall quality and performance [29,30].

The inherent strength of the extruded material filament forms the basis for the overall structural integrity and stability of 3D-printed components [31,32]. Meanwhile, Tay et al. [33] indicated that the mechanical properties of the unitary extrusion filament are based on the inherent characteristics of the materials. Enhancing the mechanical properties of the unitary extrusion filament can be achieved by optimizing the mix ratio of 3D-printing materials or incorporating fibers into the mix [24,34,35]. Nonetheless, these improvements might compromise the bond strength between layers, as previously highlighted. Nematollahi et al. [36] conducted a comparative study on 3D-printed samples, respectively employing polyvinyl alcohol (PVA), polypropylene (PP), and polyphenylene benzobisoxazole (PBO). Among these, the printed samples using PVA fibers resulted in the lowest reduction in bond strength. The layer-by-layer installation of reinforcements and the parallel integration of multiple-group yarn in the interfaces between interlayers can boost the mechanical properties of the unitary extrusion filament, mitigating the reduction in interlayer bond strength [37,38]. Despite these enhancements, the cost savings of materials or the extrusion-forming capacity were sacrificed [39,40]. Besides, a unitary external enhancement strategy may offer limited improvement to the mechanical properties in the direction of interfaces between interlayers, or may introduce certain challenges, such as feasibility and cost [41,42].

The printing path in 3D-printed concrete crucially influences the interlayer bond strength, force distribution, internal material structure, and component anisotropy, which determines the strength and stability of the final structure [43,44]. Jiang et al. [45] demonstrated that employing an arched path significantly enhanced the flexural strength of the specimens by modifying the force distribution. Battaglia et al. [46] discovered that an inter-

laced printing path facilitated a more even and dense fill, diminishing the presence of voids and discontinuities within the 3D-printed concrete. Moreover, optimizing the printing path can reduce the negative impact of anisotropy, thereby enhancing the overall performance and durability of the printed structure [47]. The printing path optimization provides an effective approach to simultaneously improving interface bonding and unlocking the full potential of printed concrete's inherent properties [48,49]. However, it poses a challenge to many previous methods because only a single material property can be improved by them [50–52].

This study aims to investigate a new approach, which reduces the effects of weak interfaces of interlayers through a spatial path layout, improving the mechanical properties of the printed structure. To evaluate the validity of this path parameter optimization, novel analytical models and parameters, including printability, mechanical properties in the unitary extrusion filament, and middle weak areas' mechanical performance between filaments, are proposed. In addition, the influence of varying material mix designs, shapes of the extrusion nozzle, equipment parameters, and programming of the printing path on the compressive strength, flexural strength, and mechanical anisotropy of 3D-printed concrete specimens are explored. Based on the proposed spatial layout of the printing path, the impact mechanisms for the printability and mechanical performance of the printing structure with various engineering parameters are investigated.

## 2. Materials and Methods

The unique control parameters of 3D-printed concrete primarily include the printing path, printing model, printing environment, and equipment parameters [53]. These four factors, respectively, affect the filling rate of printed specimens, the deposition time difference between layers, the open time of materials, and the morphology of the extruded filaments. Consequently, the size and strength of weak interlayer areas are influenced, which ultimately impacts the mechanical properties of the printed specimens.

Figure 1 illustrates the flow chart for the investigation of the proposed spatial path layout. To evaluate the effectiveness of the newly proposed method, the initial step involved constructing an analytical model during the printing process. Subsequently, the printing design parameters were determined, including the environmental factors, curing conditions, printing path interval, and layer height. Following the specifications of the design parameters for printing, both the optimized printing parameters and the coordinated condition combination were effectively implemented. Ultimately, the apparent quality, compressive strength, flexural strength, and anisotropy of printed specimens under various material mix ratios, extruder nozzle shapes, and path layouts were explored.

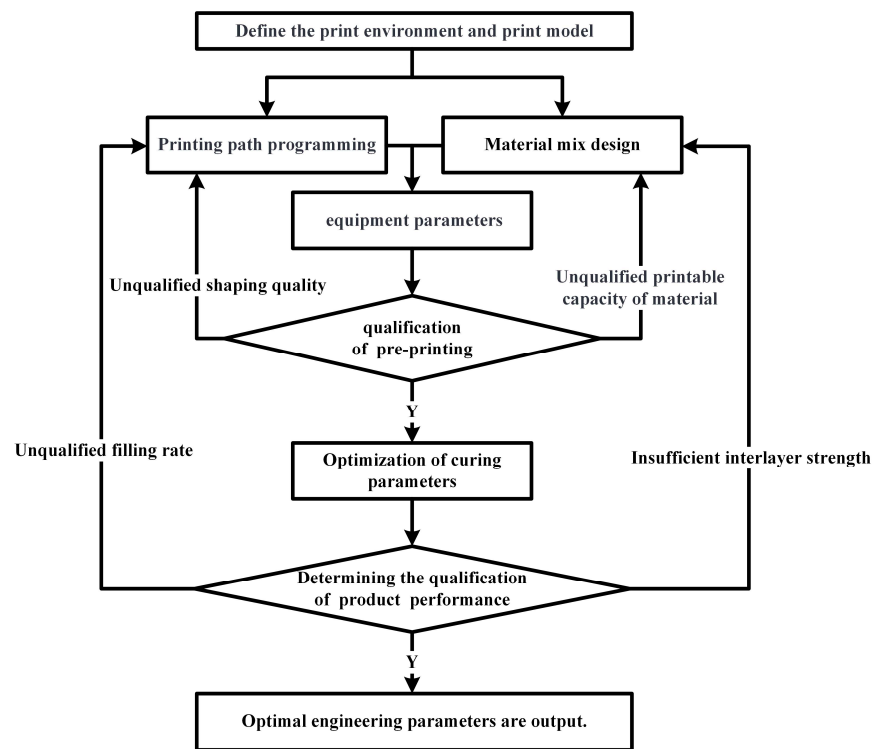


**Figure 1.** Flow chart of the investigation of the proposed spatial path layout.

### 2.1. Raw Materials

The primary raw materials utilized in the study included Portland cement (42.5R), fly ash (FA) of class F, ground granulated blast furnace slag (GGBS), and silica fume (SF), as depicted in Figure 2. FA, SF, and GGBS were employed for partial substitution of the cement, aligning with sustainability principles. Table 1 describes the details of the physical properties, chemical composition, and content of each material. In this study, the quartz sand had a particle size distribution of 1.18–2.36 mm, 0.6–1.18 mm, and 0.3–0.6 mm, with proportions of 55%, 24.8%, and 20.2%, respectively. The highly efficient polycarboxylic acid type, as a water-reducing agent, was utilized in this experiment to increase the mortar workability. The 4W-viscosity hydroxypropyl methylcellulose and polyethylene fiber (corresponding parameters are presented in Table 2) were suggested to be used in the test.

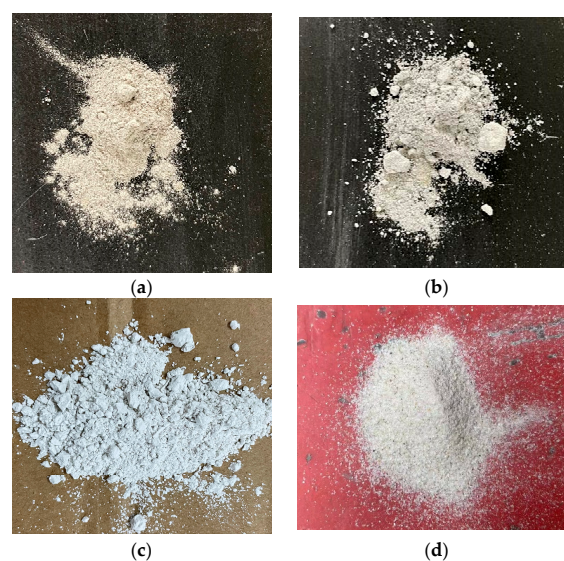


**Figure 2.** (a) FA, (b) SF, (c) GGBS, and (d) quartz sand used.

**Table 1.** Relevant physical and chemical parameters.

Precursors	Content (wt%)									Specific Surface Area (m <sup>2</sup> /kg)	Fineness of 45 μm Sieve Residue (%)	Specific Gravity
	SiO <sub>2</sub>	Loss	MgO	SO <sub>3</sub>	K <sub>2</sub> O	Na <sub>2</sub> O	Cl <sup>-</sup>	C	CaO			
Cement	19.4–21.5	4.1–4.9	2.8–2.9	61.9–64.2	1.9–2.0	1.1–1.2	3.0–3.2	0.6–0.7	0.1–0.2	350–400	-	3.0–3.1
FA	43–54	28–34	8–13	0.4–0.5	1.6–4.7	1.1–2.3	0.5–1.2	2–4	0.8–1.5	-	6.7	2.5–2.6
SF	93–97	-	-	0.26–0.28	1.0–1.1	-	-	-	-	20,000–27,000	2.2	2.1–2.2
GGBS	34.7–38.2	9.1–10.2	0.5–0.7	38.8–40.5	0.6–0.8	9.9–11.1	0.1–1.8	0.12–0.14	0.24–0.29	420–480	-	2.8–2.9

**Table 2.** Main properties of the PVA fibers.

Diameter (μm)	Length (mm)	Density (kg/m <sup>3</sup> )	Elastic Modulus (GPa)	Tensile Strength (MPa)	Elongation (%)
39	18	1.2	76.5	1950	6

## 2.2. Analytical Models

To explicitly analyze the differences in the shaping process of 3DPC, a reference coordinate system was established. In this system, the horizontal printing platform is defined as the LW plane, and the H direction is perpendicular to the horizontal printing platform. Moreover, the L, W, and H directions represent the length, width, and height of the component model, respectively. Based on the coordinate system described above, the XYZ sub-coordinate system was established, with its origin at the point where the printing nozzle extrudes the filament. Additionally, X is the direction perpendicular to the cross-section of the printing filament within the horizontal plane, Y is the direction perpendicular to the side of the printing filament in the horizontal plane, and Z is the direction perpendicular to the XY plane. Schematic diagrams of the LWH, XYZ analytical coordinate system and the weak-area distribution of the printed component are presented in Figure 3.

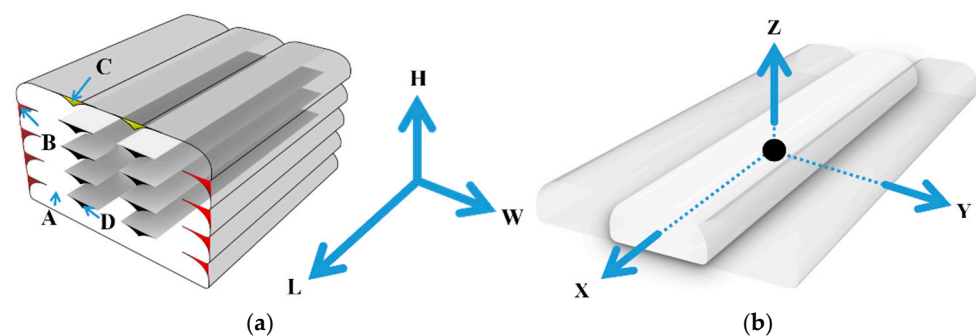


**Figure 3.** (a) Theoretical diagram of weak area inside the extrusion filament (A area), weak area in the middle of extrusion filaments (B, C, and D areas), and the LWH analytical coordinate system. (b) XYZ analytical coordinate system.

The A area represents the inner region of the printable filament. Besides, its performance is highly related to the inherent mechanical properties of the materials, representing the mechanical properties in the unitary extrusion filament. The areas of B, C, and D represent weak areas, which are in the middle of adjacent printable filaments. Further, their performance is closely linked to the bond strength of interlayer weak areas, denoting the mechanical performance of middle weak areas between filaments.

## 2.3. Optimized Spatial Path Programming Method

The 3D-printed components utilizing traditional path programming normally feature consistent counts of extrusion filaments for each layer and uniform intervals between adjacent extrusion filaments within the same layer, as shown in Figure 4a. This spatial path planning is prone to the formation of continuous interlayer weak zones in horizontal and

vertical extrusion filament structures. To enhance the compactness of components, this paper proposes a novel method for improving the mechanical performance of 3D-printed components through path optimization. This approach employs spatial path arrangements to fill construction defects caused by the printing process, thereby preventing the emergence of continuous interlayer weak interfaces at the structural level, as illustrated in Figure 4b. This partitioning is based on engineering parameters, such as component dimensions, nozzle size, and the required curing performance.

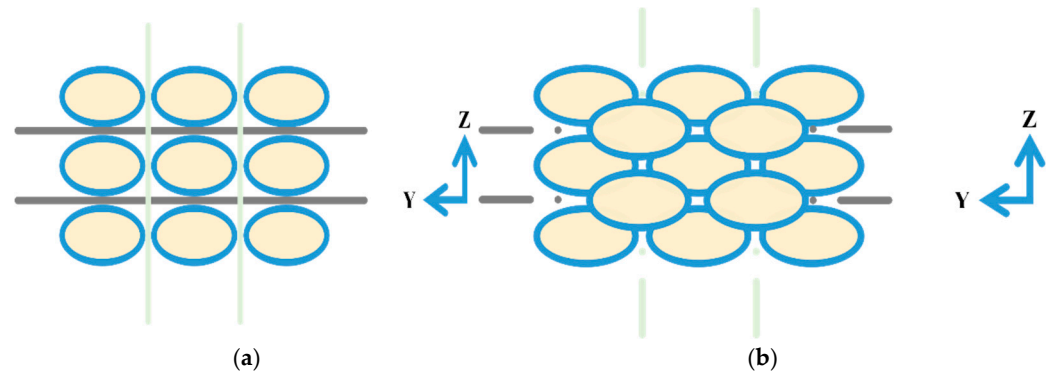


**Figure 4.** Comparison diagrammatic sketch of (a) the optimized spatial path programming method and (b) the traditional path programming method.

The proposed method focuses on dividing the print model into  $N$  combinatorial layers. The basic mode of single combinatorial layers maintains consistent printed paths and interlayer structures, as depicted in Figure 2. The intermediate extrusion filament 2 is positioned between the adjacent basic layer extrusion filament 1. The intermediate extrusion filament 2 serves as a filling to bridge the gaps between the adjacent extrusion filaments of the basic layer. Besides, the basic layer extrusion filament 1 possesses the same size as the intermediate layer extrusion filament 2. The solid points in Figure 5 represent the center cross-section of the printing path.

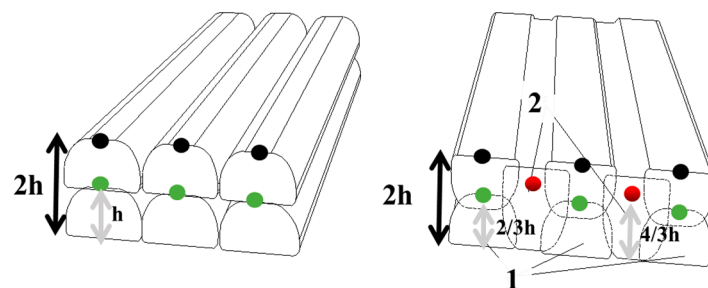


**Figure 5.** The basic mode diagrammatic sketch of the optimized spatial path programming method.  $h$  refers to the layer height of a single filament in the  $N$ -path design, with a specific value of 15 mm.

#### 2.4. Experiment Scheme Establishment

In this experiment, the proportion of cementitious materials was set at 100 weight percent (wt%). Relative to the cementitious materials, the proportions of sand and water were 130 wt% and 36 wt%, respectively. Moreover, the M1 and M2 mix proportions of 3D-printed cement were employed, as shown in Table 3. The compressive strength tests complied with the Standard Test Method of Chinese Criterion GB/T 50081-2002 [54], and the results are shown in Table 4. The compressive strength of the concrete samples using the M1 and M2 mix designs, respectively, met the standards of C40 and C60, according to the Chinese Standard GB 50010-2010 [55]. Moreover, the addition of PVA fibers, hydroxypropyl methylcellulose (HPMC), and water reducer at dosages of 0.21 wt%, 0.016 wt%, and 0.23 wt%, respectively, enhanced the workability and water retention properties of the

mortar. The length and content of fiber were selected based on experimental results and market considerations, balancing crack control, workability, and cost-effectiveness.

**Table 3.** Control mix proportion of this test.

	Components (wt%)									
	Cement	FA	SF	GGBS	Sand	Water	Water Reducer	PVA Fiber	Hydroxypropyl Methylcellulose	Calcium Formate
M1	56	10	15	20	130	36	0.23	0.21	0.016	\
M2	56	20	15	20	130	36	0.23	0.21	0.016	3.75

**Table 4.** The mechanical properties of casting samples using M1 and M2 mix proportions.

	Compressive Strength (MPa)					Flexural Strength (MPa)				
	Test 1	Test 2	Test 3	Average	SD	Test 1	Test 2	Test 3	Average	SD
M1 <sub>cast</sub>	55.5	48.2	54.4	52.7	3.94	11.2	12.3	11.6	11.7	2.87
M2 <sub>cast</sub>	68.9	70.4	74.6	71.3	0.56	13.9	12.6	13.4	13.3	2.87

For this experiment, the circular nozzle had a diameter of 28 mm, while the dimensions of the rectangular nozzle were 15 mm × 40 mm, as shown in Figure 6. Multiple trials were conducted to determine that the recommended interval between the adjacent horizontal printed paths of the components employing a circular nozzle and rectangular nozzle should be 30 mm and 38 mm, respectively.

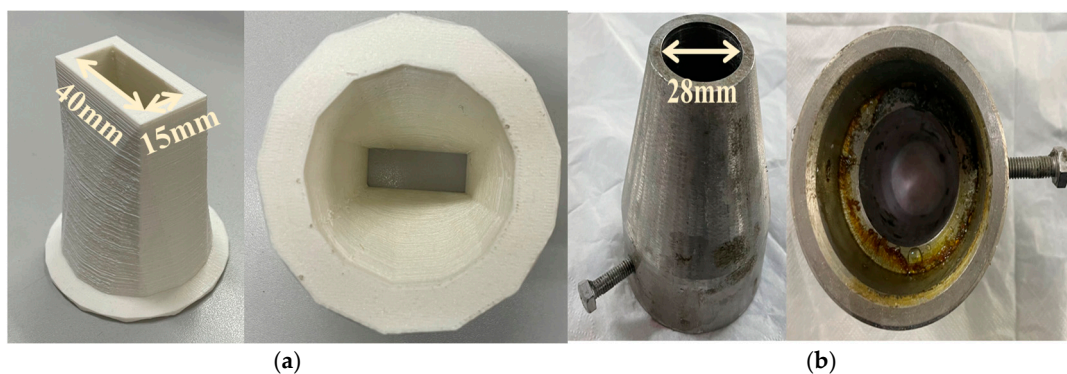


**Figure 6.** (a) Rectangular nozzle with a size of 15 mm × 40 mm. (b) Circular nozzle with a diameter of 28 mm.

In the existing technology, the majority of 3D-printed components are fabricated using a layer-by-layer deposit approach. For the extruded concrete filament of the lower and upper layers, their central axes may have deviations. The continuous or discontinuous paths between layers are set. In this experiment, the model dimensions for evaluating the apparent quality and compressive strength were designed to be 400 mm × 150 mm × 150 mm. Additionally, the model dimensions for flexural testing were designed to be 400 mm × 400 mm × 210 mm. All of the printing paths were continuous in the above model design. Staggered paths,  $S_W$  and  $S_L$ , were designed based on the spatial path planning concept in the proposed method, apart from the conventional paths,  $N_W$  and  $N_L$ . Besides, the difference between  $S_W$  and  $S_L$  lies in the direction of their path inflections, as shown in Figure 7. The layer height for the model using path S and path N was 10 mm and 15 mm, respectively, as illustrated in Figure 5. The specific path directions for the model using path S are shown in Figure 7c,d.

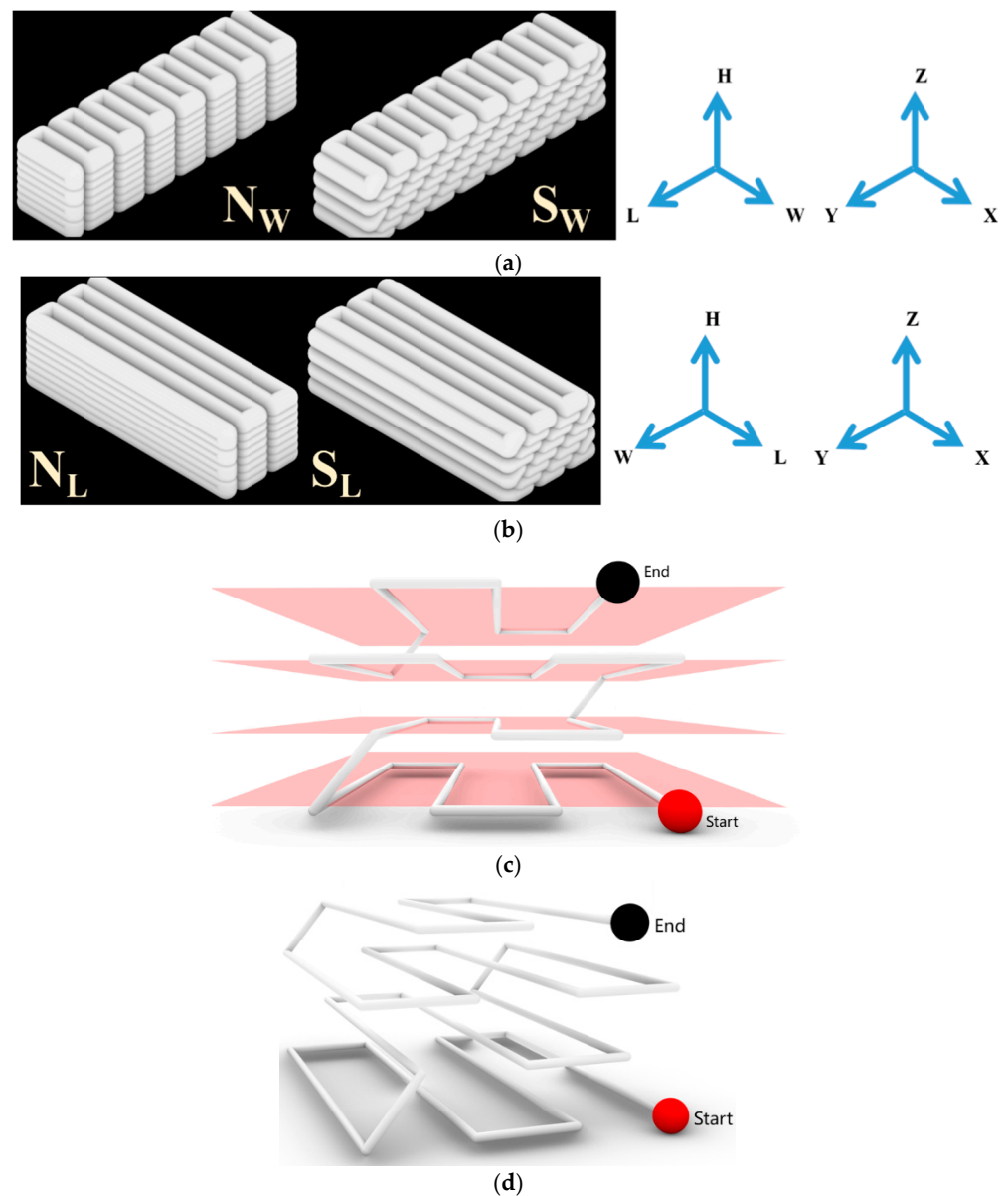


**Figure 7.** Model diagram of path inflection point directions: W (a) and L (b–d) are the trends of the staggered path, S.

The walking speed, material mixing quantity per batch, length of the pumping pipeline, and diameter of the pumping pipeline were 10 cm/s, 100 kg, 10 m, and 25 mm. Besides, the material flow rate of the per unit time was regulated by manipulating the pumping speed. Based on multiple experiments, the pumping speed was set at 8 R/min and 10 R/min, where R/min denotes the rotational speed of the pumping equipment. To ensure the accuracy of the experimental data and results, the environmental conditions during the printing process were maintained at  $14.5 \pm 1$  °C and  $75 \pm 10\%$  relative humidity, respectively, as depicted in Figure 8. During the process, the apparent quality of the printed components under different engineering parameters was compared. Specifically, experimental groups 2 and 5–10, using M1 material (a total of 7 groups), were used for the comparison of apparent quality. The compressive strength tests and flexural strength tests were conducted in groups 1–7 and groups 1–4 and 6, respectively. The specific experimental groups are presented in Table 5.



**Figure 8.** Temperature and humidity during the printing process.

**Table 5.** Printing parameters for different test groups.

Test Group	Nozzle Shape	Path	Material Types	Pump Speed
1	Circular	S <sub>W</sub>	M2	10 R/min
2	Circular	S <sub>W</sub>	M1	10 R/min
3	Circular	S <sub>W</sub>	M2	8 R/min
4	Circular	N <sub>W</sub>	M2	10 R/min
5	Circular	S <sub>L</sub>	M1	10 R/min
6	Rectangular	N <sub>W</sub>	M1	10 R/min
7	Circular	N <sub>W</sub>	M1	10 R/min
8	Circular	S <sub>W</sub>	M1	8 R/min
9	Circular	S <sub>L</sub>	M1	8 R/min
10	Circular	N <sub>L</sub>	M1	10 R/min

This experiment was conducted by changing one variable at a time and conducting pairwise comparisons.

### 2.5. Mechanical Performance Test

The experimental design was conducted in strict accordance with the Chinese Standard GB/T 50082-2009 [56] and the methodology proposed by Luo et al. [57]. The material types and nozzle shapes of the printed materials are shown in Table 5 for the mechanical performance test. The structure was extruded and deposited by 3DCP equipment based on the designative printing path, as shown in Figure 9a. The printer nozzle movement velocity was 12 cm/s, while the width and height of the shaped printing filament were 40 mm and 13 mm, respectively. Simultaneously, 5 successive roundtrip paths fabricated a layer, and 20 longitudinal layers were deposited to manufacture a printed structure.

The compressive test samples (100 mm × 100 mm × 100 mm) and the flexural test specimens (50 mm × 50 mm × 200 mm) were obtained by printed components when their on-site curing time from the start to the cutting process is 8 h, as shown in Figure 9a–c. Specifically, the cutting methods are illustrated in Figure 9f,g. The average curing temperature and humidity were 20 °C and 70%, respectively. Subsequently, the uniaxial compressive strength of X, Y, and Z directions was determined by compression tests, in which each group contained three cube specimens, respectively. The equipment employed for the compressive strength test is shown in Figure 9d. Furthermore, the flexural strength of the 3D-printed specimens was evaluated using a three-point bending test conducted on a universal testing machine, with the loading rate set at 0.05 MPa/s until failure. Each group of flexural and tensile capacity tests contained six prismatic specimens to be tested under flexural and tensile loads of XY, XZ, YX, YZ, ZX, and ZY directions, respectively, as shown in Figure 10.

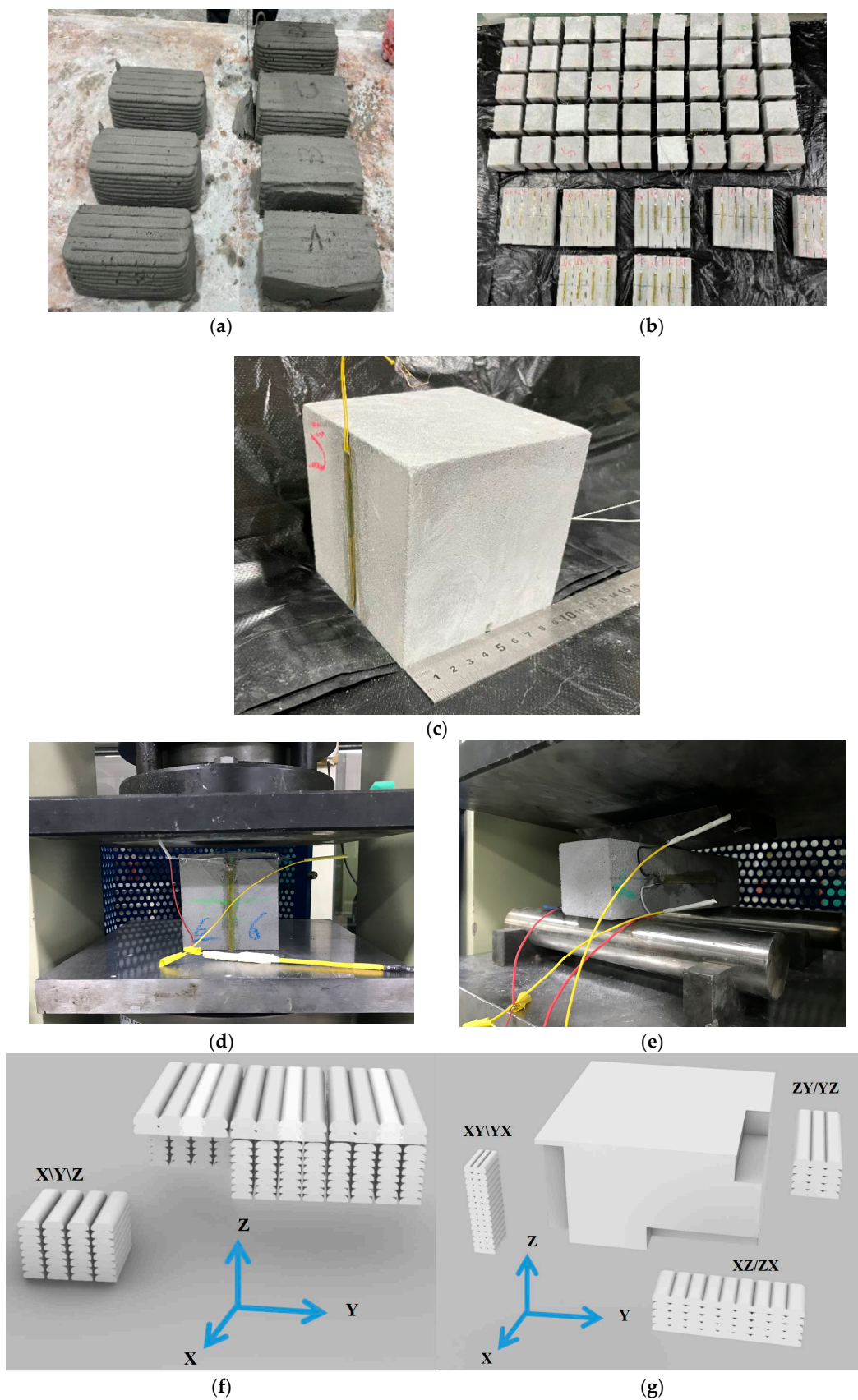


**Figure 9.** (a) Printed component and path, (b) specimen type, (c) specimen size, (d) compressive test, (e) flexural test, (f) block model for compressive test, and (g) block model for flexural test.

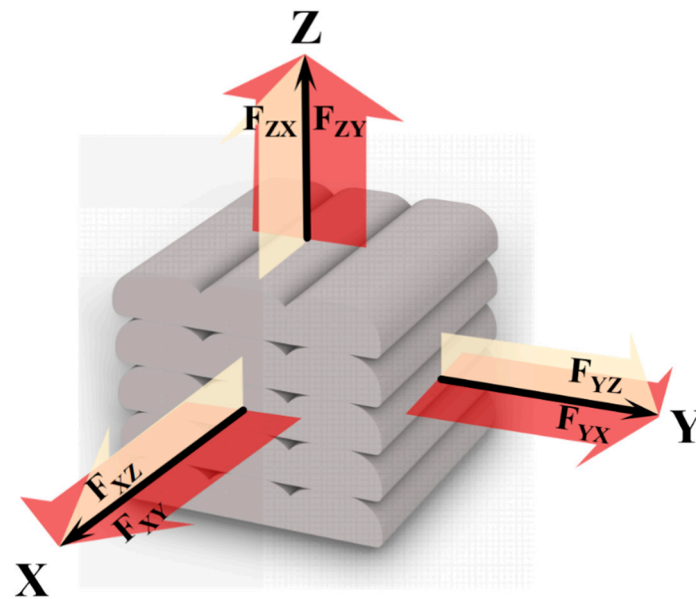


**Figure 10.** Loading direction diagrammatic sketch.

### 2.6. Anisotropy Assessment

This study applied an anisotropy coefficient to represent the influence of the printing process on the mechanical behavior of materials, as described in Equations (1) and (2) [58]:

$$f_{avg} = \frac{\sum_{n=1}^i f_{xn} + \sum_{n=1}^i f_{yn} + \sum_{n=1}^i f_{zn}}{3i} \quad (1)$$

$$I_a = \frac{\sqrt{(f_{x1} - f_{avg})^2 + \dots + (f_{xi} - f_{avg})^2 + (f_{y1} - f_{avg})^2 + \dots + (f_{yi} - f_{avg})^2 + (f_{z1} - f_{avg})^2 + \dots + (f_{zi} - f_{avg})^2}}{f_{avg}} \quad (2)$$

where  $i$  means the number of load directions in the direction of the main load,  $f_{x_i}$ ,  $f_{y_i}$ , and  $f_{z_i}$ , respectively, represent the average strength of the  $i$ -th load direction in the X, Y, and Z directions,  $f_{avg}$  demonstrates the average strength of all loads, and  $I_a$  denotes the anisotropy coefficient.

The value of  $I_a$  had a positive correlation with the anisotropy of the printed material. A smaller value of  $I_a$  ought to be employed to improve the feasibility of printed structures when the requirements for directions of mechanical properties of the structures are not determined.

## 3. Results and Discussion

### 3.1. Apparent Quality Analysis

To specifically assess the factors influencing the apparent quality, pairwise comparisons were conducted using M1 as the control mix design of the material. For pairwise comparisons of 3D-printed samples designed with path N (groups 6, 7, and 10), the effects of different corner angles and nozzle shapes on apparent quality were evaluated. For 3D-printed samples designed with the S-path (groups 5, 9, 2, and 8), pairwise comparisons focused on the effects of varying pumping speeds and corner directions on the apparent quality of the 3D-printed samples.

The apparent quality of groups 6, 7, and 10 for the N-path is shown in Figure 11. The components printed with a rectangular nozzle exhibited obvious edges, stable material extrusion, and compact interlayer bonding in the comparison of groups 6 and 7 with different extrusion nozzle shapes. Using the rectangular-shaped nozzle, the disturbance between layers after extrusion was removed because the upper-layer filament was compressed and

spread evenly onto the lower-layer filament. Therefore, the overall product printed by the rectangular nozzle achieved high-quality formation.

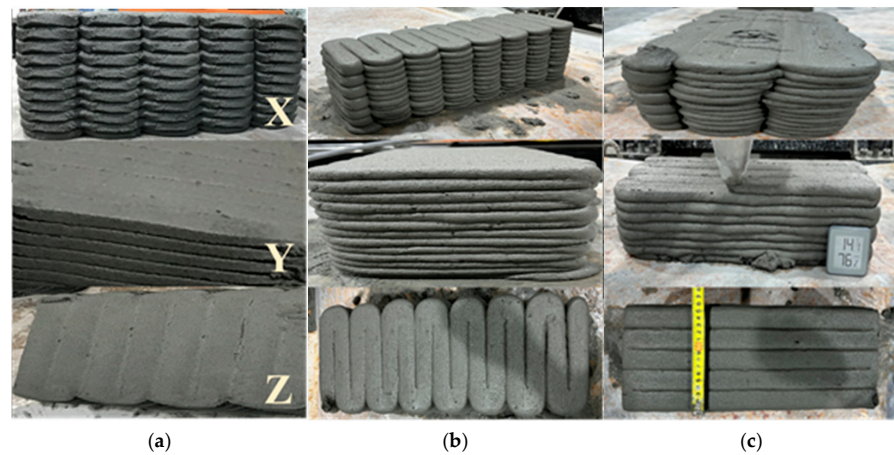


**Figure 11.** Comparison of apparent quality among the printed samples from (a) group 6, (b) group 7, and (c) group 10 employed the N-path design.

Comparing group 7 and group 10 designed with the N-path and different corner directions, group 7 demonstrated a superior apparent quality in the X direction. On the other hand, the model's repeatability in the Z direction was higher in group 10. Group 7 and group 10 both exhibited varying degrees of inhomogeneous squeezing in the Y direction because the shape of the circular nozzle had no mechanical improvement to stabilize the lateral expansion. Additionally, the rheological properties with different curing times or the nonhomogeneous features of the material contributed to significant dispersion in squeezing between lateral filaments, material compactness, and squeezing between vertical filament interlayers. The models using the corner direction W were superior to the models using the corner direction L.

Compared with groups 5, 9, 2, and 8 designed with the S-path and different pumping speeds, the apparent quality improved significantly at the pumping speed of 8 R/min. When the pumping speed was set to 10 R/min, excessive material extrusion caused significant compression between the layers and notable deviation from the intended dimensions of the printed components. Additionally, the components exhibited irregular protrusions at the center of the printed layers in the Y direction due to excessive material accumulation, as illustrated in Figure 13. In conclusion, the components using a pumping speed of 8 R/min demonstrated superior apparent quality compared to those using a pumping speed of 10 R/min.



(a)

**Figure 12.** Cont.

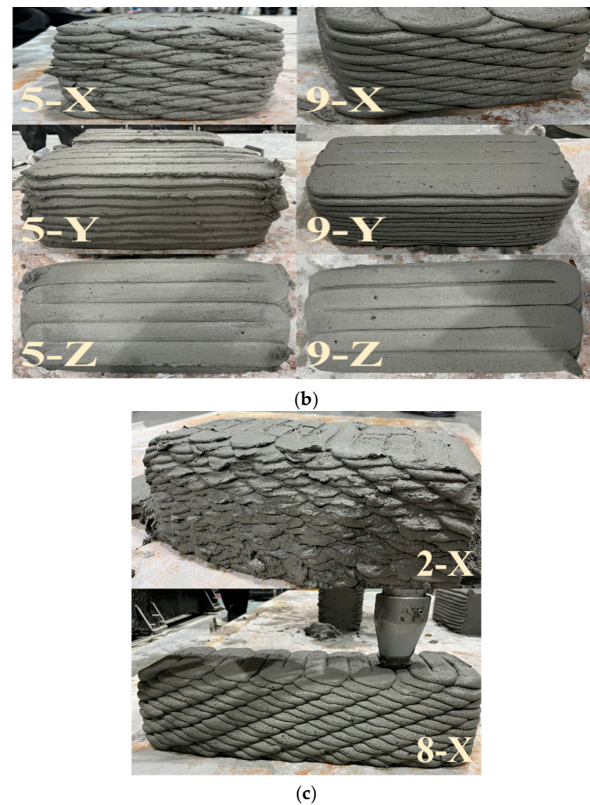


**Figure 13.** The comparison of apparent quality among specimens from groups 5, 9, 2, and 8, all designed with the S-path and varying pumping speeds: (a) apparent during the printed process, (b) comparison between groups 5 and 9, (c) comparison between groups 2 and 8.

### 3.2. Compressive Performance Analysis

The groups selected for analysis of compressive performance were designated as groups 1–7, as shown in Table 6. In the compressive strength experiments, pairwise comparisons were conducted among groups 1, 4, 2, and 7 to evaluate the optimization effects of different printing paths and materials in the 3D-printed samples. The pairwise comparisons among groups 1 and 3, groups 2 and 5, and groups 6 and 7 were used to assess the optimization effects of different pump speeds, corner directions, and nozzle shapes on the compressive strength of the 3D-printed samples, respectively.

**Table 6.** Compressive test data from different groups and directions based on the XYZ coordinate system.

Test Groups	Xi				Yi				Zi			
	C1	C2	C3	Average	C1	C2	C3	Average	C1	C2	C3	Average
1	72.8	68.4	70.4	70.53	67.4	67.6	68.4	67.80	78.4	78.8	74.4	77.20
2	56.7	57.5	64.5	59.57	50.2	58.5	60.2	56.30	65.4	64.2	62.6	64.07
3	69.6	70.9	68.9	69.80	75.5	64.3	63.6	67.80	73.9	82.7	70.9	75.83
4	50.0	61.2	50.9	54.03	53.5	67.5	60.9	60.63	52.8	46.9	52.8	50.83
5	64.2	58.1	56.1	59.47	61.6	56.9	54.5	57.67	62.0	69.0	66.6	65.87
6	52.3	48.3	43.7	48.10	56.7	50.4	61.8	56.30	39.4	33.2	33.3	35.30
7	42.6	40.5	40.2	41.10	51.1	52.0	45.7	49.60	44.3	42.6	50.5	45.80
Cast 1		55.5				48.2				54.4		
Cast 2		68.9				70.4				74.6		

Note. Here, C stands for cube.

The compressive strength test results for the different test groups in each direction are presented in Table 6. For the samples that were designed with the same printing path, the mechanical properties in different directions followed a consistent ranking. The order of

mechanical properties for specimens using the S-path (groups 1, 2, 3, and 5) and N-path (groups 4, 6, and 7) was  $Z > X > Y$  and  $Y > X > Z$ , respectively. The samples of S experienced significant weight from the extrusion filament and mechanical compression, resulting in a higher density compared to the samples of N in the Z direction. The test results comparing the mechanical performance of specimens printed by different parameters with the average values of cast specimens are illustrated in Figures 14 and 15. For the printed components that were designed with the N-path (groups 4, 6, and 7) and S-path (groups 1, 2, 3, and 5), the proportions of mechanical properties between the printed samples and the cast specimens were 0.77, 0.88, and 0.86, and 1.01, 1.14, 0.99, and 1.16, respectively. The printing pattern using the S-path produced a denser spatial distribution of printed filaments.

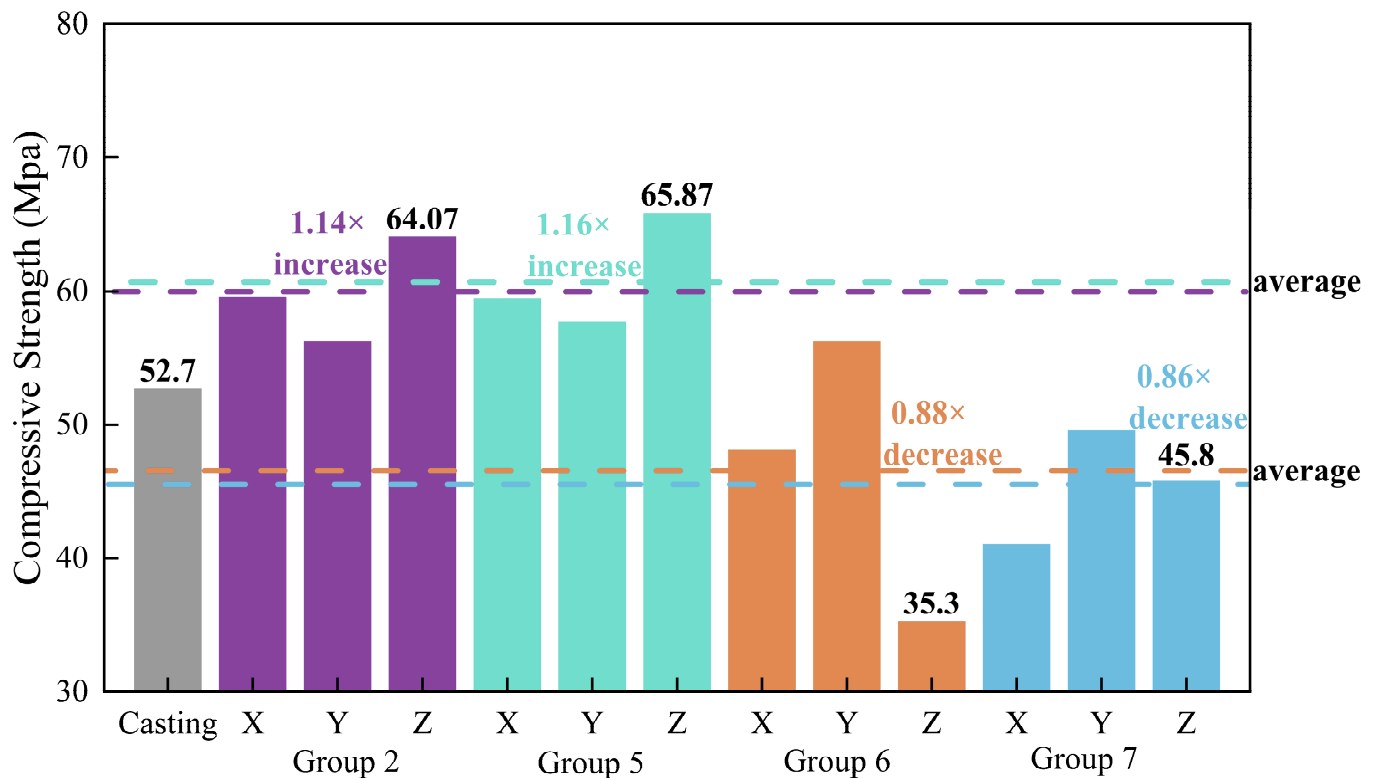


**Figure 14.** The comparison of the mechanical performance between printed specimens with S-path design (groups 2 and 5) and N-path design (groups 6 and 7) and cast specimens under different parameters based on the M1 mix proportions.

Figures 14 and 15 shows the proportion relationships between the average compressive strength in varying directions of the printed specimens and the compressive strength of the cast sample. For the M1 material (groups 2, 5, 6, and 7), the proportions were 1.14, 1.16, 0.88, and 0.86, respectively. For the M2 material (groups 1, 3, and 4), the proportions were 1.01, 0.99, and 0.77, respectively. The proportion comparison between printed samples and casting specimens indicated that the compressive strength of the printed specimen that had a higher casting compressive strength was reduced more. The increased mechanical property in the unitary extrusion filament led to denser material in the middle weak areas between filaments.

M2's sand-to-binder ratio was 1.17, which is lower than M1 (1.3). The augmented FA content replaced missing particle sizes, filling the voids among cement particles for denser extruded filaments. Simultaneously, the FA exhibited a morphological effect, allowing the extrusion filaments to obtain lateral expansion under the material's weight, compensating for the weaker mobility of the material due to the lower water-binder ratio. The lateral expansion of extrusion filaments contributed to the enhancement of macro-level

density in the printed components. The process enhanced middle weak areas' mechanical performance between filaments to diminish the effect of the printing path optimization.

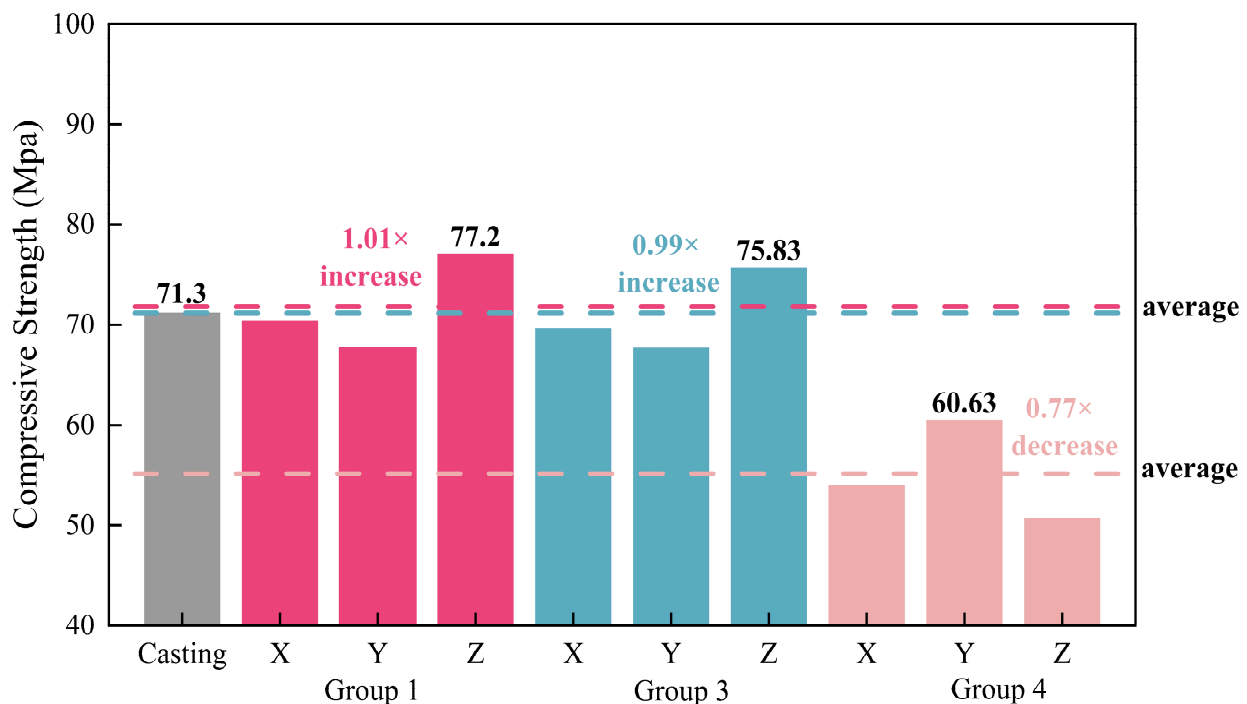


**Figure 15.** The comparison of the mechanical performance between printed specimens with S-path design (groups 1 and 3) and N-path design (group 4) and cast specimens under different parameters based on the M2 mix proportions.

In the compressive strength tests, the mechanical performance of groups 1 and 4 was generally stronger compared to groups 2 and 7 in varying directions, as shown in Table 6. The mechanical performance of the printed components became stronger as the mechanical property in the unitary extrusion filament increased with the same printing parameters, apart from the printing path.

Comparing group 1 and group 3, which were designed with different pumping speeds, a minor difference existed between the components' performance of group 1 and group 3 in each direction. The specimens were manufactured at a pumping speed of 10 R/min, obtaining slightly poorer apparent quality compared to the components printed at 8 R/min. The density of the printed components printed at different pumping speeds exhibited slight variation due to mutual internal compression. Hence, the increase in the pumping speed did not enhance the middle weak areas' mechanical performance between filaments. Consequently, a pumping speed of 8 R/min emerged as the optimal selection.

Comparing groups 2 and 5, which have different path corner directions, the mechanical performance of the same printed model was changed with X-direction movement. Thereby, this preferred direction movement can be selected, resulting in the optimal mechanical properties.

Components in group 6 and group 7 were printed using a rectangular squeezing nozzle and a circular squeezing nozzle, respectively. The mechanical performances in different directions of group 6 and group 7 were arranged as  $Y > X > Z$  and  $X > Z > Y$ , respectively. A circular squeezing nozzle should be employed when the compression strength in the Z or X direction is required for the project.

To explore the influence on middle weak areas' mechanical performance between filaments printed by the S-path, the behaviors under various loading directions using material M2 were tested. The cracks in various directions for groups 1 and 4 are demonstrated in Figure 16a. At the load threshold, group 4 exhibited distinct fracture behaviors: Multiple

sections fractured along the weaker regions between Y extrusion strands in the X direction, failure progressed through the interlayer collapse in the Y direction, and the fractures segmented into three parts along the horizontal strands' weak zones in the Z direction. Cracks began in the weak zones between filaments, extending horizontally or vertically to the point of failure. This pattern was most evident in the X direction. In contrast, group 1 did not exhibit this pattern because the core of the material was undamaged, apart from the fragmentation and delamination of its exterior. The reinforcing and toughening characteristics of the fibers were effectively developed due to the continuous and alternating arrangement of fibers along the path. Furthermore, as shown in Figure 16b, the failure surfaces in different directions for groups 1 and 4 are presented. The core concrete in group 1 designed using the S-path was effectively constrained, enhancing its ultimate bearing capacity. Meanwhile, the failure surfaces of group 4 exhibited a clear layered division along its weak zones. This contrast indicated that the optimized S-path improved the internal cohesion of the printed specimens, mitigating the mechanical performance reduction caused by weak regions between the filaments. The S-path design incorporated additional printing layers in the weak interlayer regions of 3D-printed samples and introduced fiber-reinforced filaments in continuous-interlayer weak zones, thereby enhancing the spatial distribution of fibers within the printed specimens.

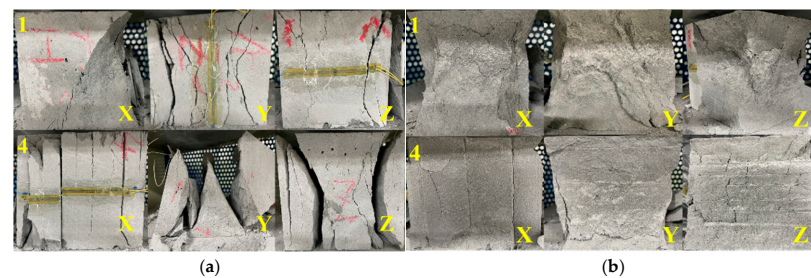


**Figure 16.** The (a) failure cracks and (b) the failure surface for printed samples from groups 1 and 4 in varying directions.

Figure 17 shows that the bearing states of the printed specimens at different stages were recorded throughout the entire failure cycle.  $T_1$  is the entire failure cycle for group 1 and  $T_4$  is for group 4. Notably, a fine crack was observed solely at  $0.6T_1$  for the components of group 1. Moreover, the crack started to slightly expand inward at  $0.8T_1$  without impacting the load-bearing capacity of the core concrete. The specimen did not completely lose its bearing capacity until  $T_1$ . In contrast, the samples of group 4 exhibited micro-cracks in a diagonal  $45^\circ$  direction at  $0.2T_4$ . Due to the increased load, the micro-cracks became increasingly obvious at  $0.6T_4$  to  $0.8T_4$ . The extension of cracks led to complete failure of the specimen at  $T_4$ , losing load-bearing capacity. The fibers in components designed with the N-path primarily influenced the interior area of extruded filaments without enhancing the middle weak areas' mechanical performance between filaments. Therefore, the fibers in components designed with the S-path exhibited a pronounced strengthening and toughening effect on the printed specimen.

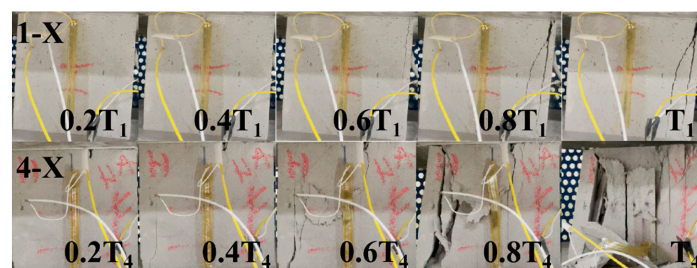


**Figure 17.** Crack propagation patterns in the X direction for printed specimens from groups 1 and 4 at different stages of the loading process.

### 3.3. Flexural Strength Analysis

The analysis of compressive strength above indicated that different corner orientations during the printed process affected the mechanical performance in various directions. Consequently, the flexural strength of the printed samples was tested based on the XYZ coordinate system to evaluate the influence of corner orientations. Based on a significant number of experiments, the groups for flexural performance analysis were designated as groups 1–4 and 6. The flexural strength tests focused on evaluating the optimization effects of different materials (groups 1 and 2) and pump speeds (groups 1 and 3) for 3D-printed samples designed with the S-path. Additionally, the same nozzle shape (groups 1 and 4) and different shapes (groups 2 and 6) of 3D-printed samples employing different path designs were compared. The flexural strength analysis was conducted on the results of the groups, as presented in Tables 7 and 8.

**Table 7.** Flexural test data of varying test groups in directions of XZ, XY, and YX.

Test Groups	XZ <sub>i</sub>			XY <sub>i</sub>			YX <sub>i</sub>		
	P1	P2	Average	P1	P2	Average	P1	P2	Average
1	10.61	8.59	9.60	7.97	8.18	8.08	7.49	8.17	7.83
2	9.36	9.82	9.59	7.83	7.76	7.80	7.20	7.85	7.53
3	10.23	10.79	10.51	8.75	8.03	8.39	8.37	8.07	8.22
4	4.45	4.12	4.29	5.06	5.45	5.26	6.34	6.17	6.26
6	5.44	5.82	5.63	9.51	9.63	9.57	6.27	5.99	6.13

**Table 8.** Flexural test data of varying test groups in directions of YZ, ZX, and ZY.

Test Groups	YZ <sub>i</sub>			ZX <sub>i</sub>			ZY <sub>i</sub>		
	P1	P2	Average	P1	P2	Average	P1	P2	Average
1	8.87	9.39	9.13	7.55	8.67	8.11	11.11	11.50	11.31
2	7.66	8.64	8.15	9.65	9.49	9.57	7.49	7.25	7.37
3	13.97	13.58	13.78	9.38	10.87	10.13	12.46	13.84	13.15
4	10.42	10.62	10.52	4.29	4.52	4.41	10.15	11.24	10.70
6	12.58	12.86	12.72	8.76	9.18	8.97	12.13	12.27	12.20

Note. Here, P stands for prism.

The average flexural strengths for the printed specimens in groups 1, 2, 3, 4, and 6 were 9.01, 8.33, 10.67, 6.90, and 9.20, respectively. The flexural strengths of the printed components were in proportion to the cast specimens. These proportions were 0.68, 0.71, 0.80, 0.52, and 0.79, respectively. The lowest average strength loss existed in specimens printed with an S-path design using a circular nozzle, at only 20%. The printed specimens designed with the N-path using the rectangular nozzle displayed a strength reduction of 21%. Figures 18 and 19 illustrates that the flexural strength in the ZY and YZ directions was higher compared to other directions. In the ZX and XZ directions, the printed samples designed with the N-path acquired 32.26–33.16% of the flexural strength of the cast specimens. Besides, 58.87–66.67% flexural strength of the cast specimens was obtained by printed samples designed with the S-path in the XY and YX directions. Using the N-path design, 48.12–52.39% flexural strength in the XZ and YX directions of the cast sample was gained by the printed specimens. This result illustrates that both the S-path and the rectangular nozzle contributed to optimizing middle weak areas' mechanical performance between filaments.

Using the circular printing nozzle, the average flexural strength of samples in group 3 with the S-path design increased by 1.55 times compared to group 4 samples with the N-path design. Meanwhile, the printed samples of group 3 exhibited improvements of 145.27% and 129.85% in the XZ and ZX directions, respectively. The average flexural strength of components also had significant optimizations in other directions. Their increased values

were 56.42%, 31.41%, 30.94%, and 22.95% in the XY, YX, YZ, and ZY directions, respectively, as shown in Figure 20.

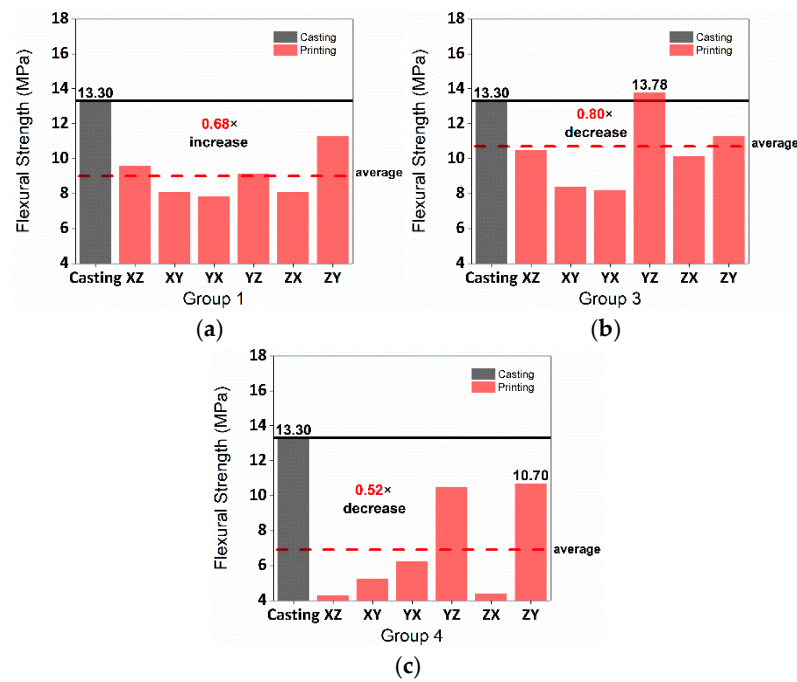


**Figure 18.** The comparison of the flexural strength between printed specimens of (a) group 1 and (b) group 3 using the S-path design and those of (c) group 4 employing the N-path design and cast specimens in varying directions based on the M2 mix proportion.

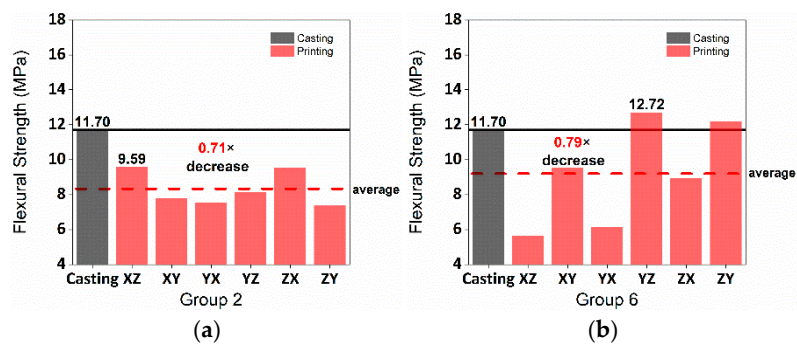


**Figure 19.** The comparison of the flexural strength between printed specimens of (a) group 2 using the S-path design and those of (b) group 6 employing the N-path design and cast specimens in varying directions based on the M1 mix proportion.

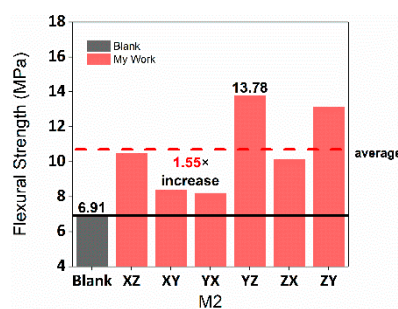


**Figure 20.** The average flexural strength comparison of the printed specimens designed with the S-path and N-path using M2 material.

From the comparison between the specimens using M2 (groups 1, 3, and 4) and M1 (groups 2 and 6), the influence of material intrinsic strength on the flexural strength of printed specimens was diminished. Despite this, the flexural strength of cast samples using M1 was 0.88 times that of specimens using M2. The average strength of the printed specimens using M1 was 0.93 times that of M2. The observations of the cut printed specimen, as depicted in Figure 21, indicated that the visibility of macroscopic defects in the printed specimens increased in the following order: groups 1 and 2, group 6, and group 4. In contrast to the compressive strength test results, the average flexural strength of the printed specimens was affected by such factors, which included the printing path, nozzle design, and pump speed.

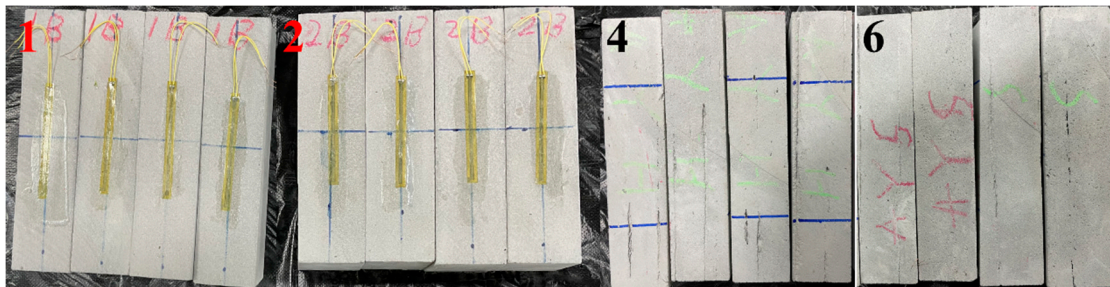


**Figure 21.** Printed specimens of groups 1, 2, 4, and 6 after cutting.

The comparison of group 1 and group 4 demonstrated that an S-path design strategy can enhance the flexural strength of specimens. Specifically, it significantly mitigated the impact of weak regions between filaments, leading to strength improvements in the XY, YX, XZ, and ZX orientations by 53.61%, 25.08%, 123.78%, and 83.90%, respectively. The continuous and staggered distribution of fibers along the S-path between layers contributed to this improvement by effectively preventing the oriented distribution of fibers within a single layer. Furthermore, the application of appropriate extrusion pressure significantly enhanced the bonding performance between adjacent extrusion filaments. The S-path design partially optimized the failure mode of printed components in the XZ direction. In the XZ direction of group 4, the failure occurred at approximately one-third of the specimen's height, displaying a brittle fracture. In group 1's XZ direction, the failure crack propagated through the middle of the specimen, while the fibers prevented complete fracture, as depicted in Figure 22. The fracture surface of group 4, as depicted in Figure 22b, showed clear printing deposition marks, flaws during the printing process, and several areas of fiber failure. The load-bearing area within the specimen was smaller than its cross-section, with fibers playing a minimal role in bearing the load.

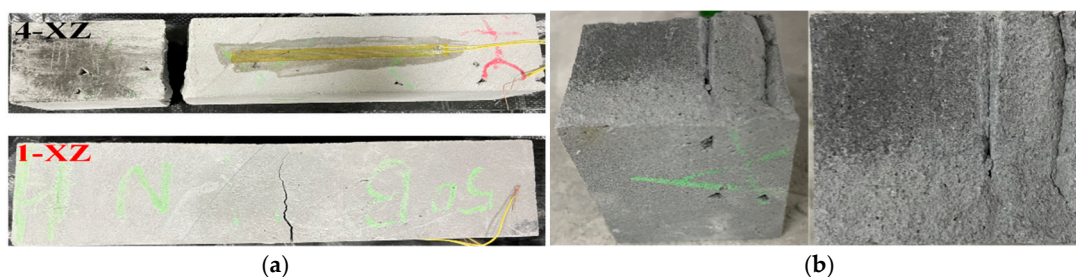


**Figure 22.** (a) Failure state of group 4 and group 1 specimens in the XZ direction, and (b) failure sections of group 4.

Using the N-path design, the average strength of the printed specimens using the M1 material and a rectangular nozzle was 1.33 times that of samples using the M2 material and a circular nozzle by comparing groups 4 and 6. During the printing process using the rectangular nozzle and the N-path design, ten samples (2000 mm × 160 mm × 104 mm rect-

angular prism) were observed, as shown in Figure 23. Mechanical compaction by the nozzle ensured uniformity in the cross-sections of the extruded filaments, leading to consistent printing materials' layer heights and stable spacing between the extruded filaments. The process had minimal impact on the adjacent extrusion filaments. Consequently, employing the rectangular nozzle could improve the tensile properties of the weak zones between the extrusion filaments, enhancing the flexural strength of the printed specimens.



**Figure 23.** Stable extrusion filaments of a rectangular nozzle in the N-path.

Group 1 and group 3 were printed with a pumping speed of 10 R/min and 8 R/min, respectively. The differences in flexural strengths from their average values in XZ, XY, YX, YZ, ZX, and ZY directions were 6.57%, 10.36%, 13.08%, 1.35%, 9.97%, and 25.49%, respectively. The flexural strength of group 1's printed samples exhibited a decrease of 0.12 compared to that of cast specimens. Among them, the flexural strengths in the YZ direction obtained the biggest loss of 4.65 MPa when the components were printed at a pumping speed of 10 R/min and a single-layer height of 10 mm. Excessive material extrusion per unit of time led to greater compaction within the printed specimen. Additionally, using the circular nozzle, which extruded the material without physical guidance, the extrusion filaments and material stretching after extrusion exhibited significant fluctuations, as illustrated in Figure 24, reducing the flexural strength in the YZ direction. Thereby, the S-path printing design and rectangular nozzle could improve the flexural strength of the printed components.

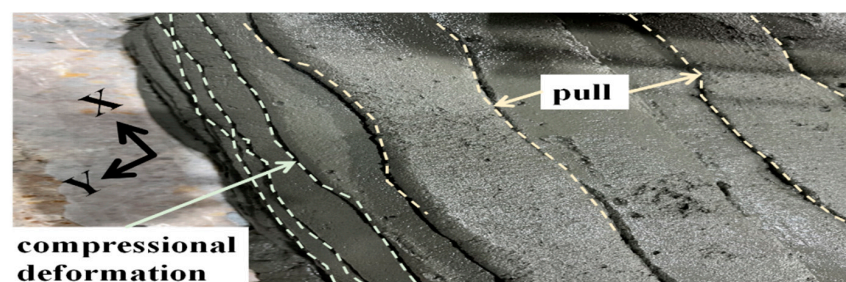


**Figure 24.** Fluctuations when a circular nozzle was used in the S-path.

### 3.4. Anisotropy Analysis

The test results of compressive and flexural performance were input into anisotropy assessment formulas, obtaining the anisotropy values of compressive and flexural capacity for various groups, as shown in Table 9 and Figure 25.

Components designed with the N-path and a rectangular nozzle demonstrated a maximum anisotropy of 32.14% compressive strength. Due to the absence of physical compression between layers and the horizontal filament interaction, the rectangular nozzle exhibited greater anisotropy. In contrast, the components of groups 1, 2, 3, and 5, which were designed with the S-path, exhibited a similar anisotropy (approximately 10%). Among them, the optimal anisotropy was found in group 3 (8.31%). The samples designed with the N-path exhibited anisotropy that was at least 2.82% higher than the components designed with the S-path. Despite various material designs and pumping speeds, compressive strength anisotropy remained stable in specimens printed with the circular nozzle and

S-path. The maximum anisotropy of flexural strength was 95.66% when the specimens were printed using the N-path design and a circular nozzle. The printing process using a circular nozzle had unstable spacing between the extruded filament, leading to larger defects. Group 2 achieved the lowest anisotropy of 26.83% when the flexural strengths of three groups designed with the S-path were compared. The higher water–cement ratio of the M1 than the M2 material contributed to the optimal anisotropy because the flowability and the density of materials obtained an increase using the S-path design. The anisotropy of flexural strength in the printed specimens was influenced by the mechanical properties in the unitary extrusion filament, printing path, extrusion nozzle shape, and pumping speed. Therefore, the S-path can play a crucial role in achieving mechanical isotropy of printed specimens. Moreover, the spatial arrangement employing the S-path design effectively prevented the emergence of continuous-interlayer weak interfaces. However, the interlayer weak regions still existed, particularly apparent in the flexural strength data. The tensile anisotropy of the printed specimens was further intensified by the inconsistent interlayer spatial arrangement, defect distribution, and inherent tensile property disparities in the concrete material.

**Table 9.** Values of compressive and flexural anisotropy of various groups.

Test Group	CS	FS
1	9.52%	32.77%
2	9.20%	26.83%
3	8.31%	48.88%
4	12.81%	95.66%
5	9.99%	\
6	32.14%	71.87%
7	13.23%	\

Note. Here, CS denotes the compressive strength, and FS denotes the flexural strength.

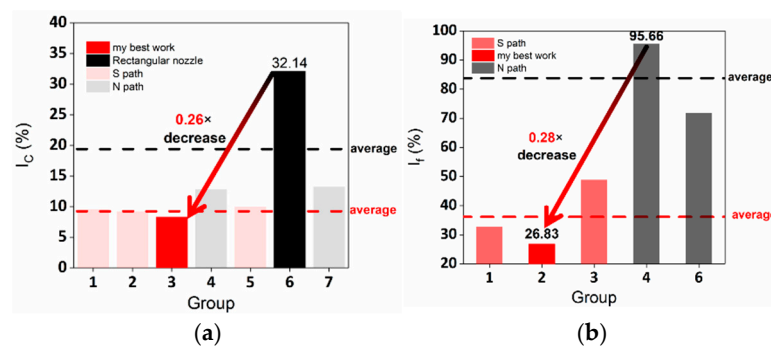


**Figure 25.** Comparison of (a) compressive and (b) bending anisotropy of each group.

#### 4. Conclusions

This study proposed an innovative printing path layout to improve the mechanical performance of components using the 3DCP technology. Six factors influencing the performance of printing components were proposed to control the printed materials' quality. Meanwhile, an engineering parameter-matching model was constructed to facilitate the effectiveness and accuracy of the experiments. The conclusions were as follows:

- (1) Using a comprehensive evaluation, which considered the nozzle shape, printed path, material properties, and pump speed, the S-path printing design was confirmed to reduce the loss of mechanical properties in the unitary extrusion filament caused by the printing technique.
- (2) The S-path design introduced additional printing layers in the weak interlayer regions of the 3D-printed samples and incorporated fiber-reinforced filaments in continuous weak zones. This method optimized the spatial distribution of fibers within the printed samples, enhancing the mechanical performance and reducing anisotropy.

- (3) The S-path design improved the compressive strength of the printed samples, achieving an average compressive strength of 72.01 MPa and reducing the anisotropy to 8.31%. Additionally, the S-path design enhanced the internal cohesion of the printed samples, thereby improving the failure mode of the printed specimens.
- (4) The S-path design improved the flexural strength of the printed samples, creating an average flexural strength of 10.71 MPa and reducing the anisotropy to 26.83%, which was higher than the control printing group. Besides, the failure mode was improved from the brittle fracture to the partial fracture.
- (5) The rectangular nozzle was used to improve the tensile properties of the weak zones between the extrusion filaments, enhancing the flexural strength of the printed specimens.

## 5. Future Research

Based on this research, the research limitations and future research were identified:

1. This study demonstrated that the application of the S-path design reduced the occurrence of weak interlayer regions in 3D-printed concrete. Quantitative analysis at the micro-level is an area for future work to further investigate the optimization degree of interlayer weak regions and fiber spatial arrangement in 3D-printed samples under the S-path design through CT scanning and interlayer bonding strength tests.
2. The mechanical tests indicated that 3D-printed samples using the S-path exhibited improved mechanical performance across various directions, materials, and equipment parameters. The Poisson effect in the printed specimens was not considered in this study. Therefore, comprehensive further research is required to explore the Poisson effect in varying directions employing a conventional triaxial testing machine equipped with circumferential LVDT sensors.
3. The mutual extrusion of interlayer materials can lead to irregular lateral expansion of the printed products. Theoretically, materials exhibit varying degrees of yield during the printing process. This study did not utilize experimental methods for real-time detection of static and dynamic yield stress. It is essential to conduct a real-time quantitative analysis of the material yield state during the printing process through specific testing methods and detection patterns.

**Author Contributions:** Conceptualization, M.Y.; Methodology, B.W., M.Y., S.L. and X.W.; Formal analysis, B.W. and S.L.; Investigation, B.W.; Resources, X.Y.; Data curation, X.L.; Writing—original draft, B.W.; Writing—review & editing, X.L. and H.Z.; Visualization, X.W.; Supervision, H.Z., Y.L. and X.Y.; Project administration, Y.L.; Funding acquisition, H.Z. All authors have read and agreed to the published version of the manuscript.

**Funding:** This research was funded by [the Innovation Capability Support Program of Shaanxi] in China, grant number [Program No. 2023-CX-TD-41].

**Institutional Review Board Statement:** Not applicable.

**Informed Consent Statement:** Not applicable.

**Data Availability Statement:** The data are available from the corresponding author, Hongyu Zhao, upon reasonable request. Please contact Hongyu Zhao at 20211601069@cqu.edu.cn.

**Conflicts of Interest:** Authors Bolin Wang, Min Yang, Shilong Liu, Yishuang Liang, Xiaofei Yao were employed by the company CCCC First Highway Consultants Co., Ltd. The remaining authors declare that the research was conducted in the absence of any commercial or financial relationships that could be construed as a potential conflict of interest.

## References

1. Ness, D. Towards sufficiency and solidarity: COP27 implications for construction and property. *Build. Cities* **2022**, *3*, 912–919. [[CrossRef](#)]
2. Yan, R.; Ma, M.; Zhou, N.; Feng, W.; Xiang, X.; Mao, C. Towards COP27: Decarbonization patterns of residential building in China and India. *Appl. Energy* **2023**, *352*, 122003. [[CrossRef](#)]

3. Lim, J.H.; Weng, Y.; Pham, Q.-C. 3D printing of curved concrete surfaces using Adaptable Membrane Formwork. *Constr. Build. Mater.* **2020**, *232*, 117075. [[CrossRef](#)]
4. Mechtcherine, V.; Grafe, J.; Nerella, V.N.; Spaniol, E.; Hertel, M.; Füssel, U. 3D-printed steel reinforcement for digital concrete construction—Manufacture, mechanical properties and bond behaviour. *Constr. Build. Mater.* **2018**, *179*, 125–137. [[CrossRef](#)]
5. Sun, J.; Aslani, F.; Wei, J.; Wang, X. Electromagnetic absorption of copper fiber oriented composite using 3D printing. *Constr. Build. Mater.* **2021**, *300*, 124026. [[CrossRef](#)]
6. Sun, J.; Lin, S.; Zhang, G.; Sun, Y.; Zhang, J.; Chen, C.; Morsy, A.M.; Wang, X. The effect of graphite and slag on electrical and mechanical properties of electrically conductive cementitious composites. *Constr. Build. Mater.* **2021**, *281*, 122606. [[CrossRef](#)]
7. Hassanin, A.; El-Nemr, A.; Shaaban, H.F.; Saidani, M.; Shaaban, I.G. Coupling behavior of autogenous and autonomous self-healing techniques for durable concrete. *Int. J. Civ. Eng.* **2024**, *22*, 925–948. [[CrossRef](#)]
8. Zhao, H.; Wang, Y.; Liu, X.; Wang, X.; Chen, Z.; Lei, Z.; Zhou, Y.; Singh, A. Review on Solid Wastes Incorporated Cementitious Material using 3D Concrete Printing Technology. *Case Stud. Constr. Mater.* **2024**, *21*, e03676. [[CrossRef](#)]
9. Agusti-Juan, I.; Müller, F.; Hack, N.; Wangler, T.; Habert, G. Potential benefits of digital fabrication for complex structures: Environmental assessment of a robotically fabricated concrete wall. *J. Clean. Prod.* **2017**, *154*, 330–340. [[CrossRef](#)]
10. Lim, S.; Buswell, R.A.; Le, T.T.; Austin, S.A.; Gibb, A.G.; Thorpe, T. Developments in construction-scale additive manufacturing processes. *Autom. Constr.* **2012**, *21*, 262–268. [[CrossRef](#)]
11. Liu, Z.; Li, M.; Weng, Y.; Wong, T.N.; Tan, M.J. Mixture Design Approach to optimize the rheological properties of the material used in 3D cementitious material printing. *Constr. Build. Mater.* **2019**, *198*, 245–255. [[CrossRef](#)]
12. Sun, J.; Huang, Y.; Aslani, F.; Ma, G. Electromagnetic wave absorbing performance of 3D printed wave-shape copper solid cementitious element. *Cem. Concr. Compos.* **2020**, *114*, 103789. [[CrossRef](#)]
13. Sun, J.; Huang, Y.; Aslani, F.; Ma, G. Properties of a double-layer EMW-absorbing structure containing a graded nano-sized absorbent combing extruded and sprayed 3D printing. *Constr. Build. Mater.* **2020**, *261*, 120031. [[CrossRef](#)]
14. Sun, J.; Aslani, F.; Lu, J.; Wang, L.; Huang, Y.; Ma, G. Fresh and mechanical behaviour of developed fibre-reinforced lightweight engineered cementitious composites for 3D concrete printing containing hollow glass microspheres. *Ceram. Int.* **2021**, *47*, 27107–27121. [[CrossRef](#)]
15. Sun, J.; Huang, Y.; Aslani, F.; Wang, X.; Ma, G. Mechanical enhancement for EMW-absorbing cementitious material using 3D concrete printing. *J. Build. Eng.* **2021**, *41*, 102763. [[CrossRef](#)]
16. Zhang, G.; Wang, J.; Jiang, Z.; Peng, C.; Sun, J.; Wang, Y.; Chen, C.; Morsy, A.M.; Wang, X. Properties of Sustainable Self-Compacting Concrete containing Activated Jute Fiber and Waste Mineral Powders. *J. Mater. Res. Technol.* **2022**, *19*, 1740–1758. [[CrossRef](#)]
17. Moelich, G.M.; Kruger, J.; Combrinck, R. Plastic shrinkage cracking in 3D printed concrete. *Compos. Part B Eng.* **2020**, *200*, 108313. [[CrossRef](#)]
18. Shakor, P.; Nejadi, S.; Paul, G. A study into the effect of different nozzles shapes and fibre-reinforcement in 3D printed mortar. *Materials* **2019**, *12*, 1708. [[CrossRef](#)] [[PubMed](#)]
19. Shaaban, I.; El Nemr, A.; Ahmed, H. Spotlight on mechanical properties of autogenic self-healing of concrete. In Proceedings of the 2nd International Summit on Civil, Structural, and Environmental Engineering, Florence, Italy, 18–20 March 2024.
20. Eddy, L.; Jiradilok, P.; Matsumoto, K.; Nagai, K. Analytical investigation of the role of reinforcement in perpendicular beams of beam-column knee joints by 3D meso-scale model. *Eng. Struct.* **2020**, *210*, 110347. [[CrossRef](#)]
21. Wolfs, R.; Bos, F.; Salet, T.J.C.; Research, C. Hardened properties of 3D printed concrete: The influence of process parameters on interlayer adhesion. *Cem. Concr. Res.* **2019**, *119*, 132–140. [[CrossRef](#)]
22. Panda, B.; Paul, S.C.; Tan, M.J. Anisotropic mechanical performance of 3D printed fiber reinforced sustainable construction material. *Mater. Lett.* **2017**, *209*, 146–149. [[CrossRef](#)]
23. Salet, T.A.; Ahmed, Z.Y.; Bos, F.P.; Laagland, H.L.; Prototyping, P. Design of a 3D printed concrete bridge by testing. *Virtual Phys. Prototyp.* **2018**, *13*, 222–236. [[CrossRef](#)]
24. Sanjayan, J.G.; Nematollahi, B.; Xia, M.; Marchment, T. Effect of surface moisture on inter-layer strength of 3D printed concrete. *Constr. Build. Mater.* **2018**, *172*, 468–475. [[CrossRef](#)]
25. Ma, G.; Sun, J.; Aslani, F.; Huang, Y.; Jiao, F. Review on electromagnetic wave absorbing capacity improvement of cementitious material. *Constr. Build. Mater.* **2020**, *262*, 120907. [[CrossRef](#)]
26. Sun, J.; Wang, Y.; Li, K.; Yao, X.; Zhu, B.; Wang, J.; Dong, Q.; Wang, X. Molecular interfacial properties and engineering performance of conductive fillers in cementitious composites. *J. Mater. Res. Technol.* **2022**, *19*, 591–604. [[CrossRef](#)]
27. Van Der Putten, J.; De Schutter, G.; Van Tittelboom, K. Surface modification as a technique to improve inter-layer bonding strength in 3D printed cementitious materials. *RILEM Tech. Lett.* **2019**, *4*, 33–38. [[CrossRef](#)]
28. Marchment, T.; Sanjayan, J.G.; Nematollahi, B.; Xia, M. Interlayer strength of 3D printed concrete: Influencing factors and method of enhancing. In *3D Concrete Printing Technology*; Elsevier: Amsterdam, The Netherlands, 2019; pp. 241–264.
29. Ding, T.; Xiao, J.; Zou, S.; Wang, Y.J.C.; Composites, C. Hardened properties of layered 3D printed concrete with recycled sand. *Cem. Concr. Compos.* **2020**, *113*, 103724. [[CrossRef](#)]
30. Meurer, M.; Classen, M.J.M. Mechanical properties of hardened 3D printed concretes and mortars—Development of a consistent experimental characterization strategy. *Materials* **2021**, *14*, 752. [[CrossRef](#)]

31. Khan, S.B.; Irfan, S.; Lam, S.S.; Sun, X.; Chen, S. 3D printed nanofiltration membrane technology for waste water distillation. *J. Water Process. Eng.* **2022**, *49*, 102958. [[CrossRef](#)]
32. Zhao, B.; Wang, G.; Wu, B.; Kong, X.J.C.; Materials, B. A study on mechanical properties and permeability of steam-cured mortar with iron-copper tailings. *Constr. Build. Mater.* **2023**, *383*, 131372. [[CrossRef](#)]
33. Tay, Y.W.; Panda, B.; Paul, S.C.; Tan, M.J.; Qian, S.Z.; Leong, K.F.; Chua, C.K. Processing and properties of construction materials for 3D printing. *Mater. Sci. Forum* **2016**, *861*, 177–181.
34. Yu, S.; Xia, M.; Sanjayan, J.; Yang, L.; Xiao, J.; Du, H. Microstructural characterization of 3D printed concrete. *J. Build. Eng.* **2021**, *44*, 102948. [[CrossRef](#)]
35. Kruger, J.; du Plessis, A.; van Zijl, G.J.A.M. An investigation into the porosity of extrusion-based 3D printed concrete. *Addit. Manuf.* **2021**, *37*, 101740. [[CrossRef](#)]
36. Nematollahi, B.; Xia, M.; Sanjayan, J.; Vijay, P. Effect of type of fiber on inter-layer bond and flexural strengths of extrusion-based 3D printed geopolymer. *Mater. Sci. Forum* **2018**, *939*, 155–162.
37. Marchment, T.; Sanjayan, J. Bond properties of reinforcing bar penetrations in 3D concrete printing. *Autom. Constr.* **2020**, *120*, 103394. [[CrossRef](#)]
38. Gebhard, L.; Mata-Falcón, J.; Anton, A.; Dillenburger, B.; Kaufmann, W. Structural behaviour of 3D printed concrete beams with various reinforcement strategies. *Eng. Struct.* **2021**, *240*, 112380. [[CrossRef](#)]
39. Liu, H.; Liu, C.; Wu, Y.; Bai, G.; He, C.; Zhang, R.; Wang, Y.J.C.; Research, C. Hardened properties of 3D printed concrete with recycled coarse aggregate. *Cem. Concr. Res.* **2022**, *159*, 106868. [[CrossRef](#)]
40. Zhang, J.; Wang, J.; Dong, S.; Yu, X.; Han, B. A review of the current progress and application of 3D printed concrete. *Compos. Part A Appl. Sci. Manuf.* **2019**, *125*, 105533. [[CrossRef](#)]
41. Li, J.; Qin, Q.; Sun, J.; Ma, Y.; Li, Q. Mechanical and conductive performance of electrically conductive cementitious composite using graphite, steel slag, and GGBS. *Struct. Concr.* **2020**, *23*, 533–547. [[CrossRef](#)]
42. Aslani, F.; Sun, J.; Huang, G. Mechanical behavior of fiber-reinforced self-compacting rubberized concrete exposed to elevated temperatures. *J. Mater. Civ. Eng.* **2019**, *31*, 04019302. [[CrossRef](#)]
43. Zhang, Y.; Huang, Z.; Wang, F.; Li, J.; Wang, H.; Insulation, E. Design of bioinspired highly aligned bamboo-mimetic metamaterials with structural and functional anisotropy. *IEEE Trans. Dielectr. Electr. Insul.* **2023**, *30*, 1170–1177. [[CrossRef](#)]
44. Alchaar, A.S.; Al-Tamimi, A.K.J.C.; Materials, B. Mechanical properties of 3D printed concrete in hot temperatures. *Constr. Build. Mater.* **2021**, *266*, 120991. [[CrossRef](#)]
45. Jiang, X.; Li, Y.; Yang, Z.; Li, Y.; Xiong, B. Harnessing Path Optimization to Enhance the Strength of Three-Dimensional (3D) Printed Concrete. *Buildings* **2024**, *14*, 455. [[CrossRef](#)]
46. Battaglia, C.A.; Miller, M.F.; Verian, K.P. Print-cast concrete: Additive manufacturing for 3D printing mortar in robotically fabricated green sand molds. In Proceedings of the Second RILEM International Conference on Concrete and Digital Fabrication: Digital Concrete 2020 2; Springer International Publishing: Cham, Switzerland, 2020; pp. 757–767.
47. Murcia, D.H.; Genedy, M.; Taha, M.R.J.C.; Materials, B. Examining the significance of infill printing pattern on the anisotropy of 3D printed concrete. *Constr. Build. Mater.* **2020**, *262*, 120559. [[CrossRef](#)]
48. Aslani, F.; Sun, J.; Bromley, D.; Ma, G. Fiber-reinforced lightweight self-compacting concrete incorporating scoria aggregates at elevated temperatures. *Struct. Concr.* **2019**, *20*, 1022–1035. [[CrossRef](#)]
49. Aslani, F.; Hou, L.; Nejadi, S.; Sun, J.; Abbasi, S. Experimental analysis of fiber-reinforced recycled aggregate self-compacting concrete using waste recycled concrete aggregates, polypropylene, and steel fibers. *Struct. Concr.* **2019**, *20*, 1670–1683. [[CrossRef](#)]
50. Tay, Y.W.D.; Ting, G.H.A.; Qian, Y.; Panda, B.; He, L.; Tan, M.J.J.V.; Prototyping, P. Time gap effect on bond strength of 3D-printed concrete. *Virtual Phys. Prototyp.* **2019**, *14*, 104–113. [[CrossRef](#)]
51. Xiao, J.; Liu, H.; Ding, T.; Ma, G.J. 3D printed concrete components and structures: An overview. *Sustain. Struct.* **2021**, *1*, 000006. [[CrossRef](#)]
52. Joh, C.; Lee, J.; Park, J.; Yang, I.-H.J.M. Buildability and mechanical properties of 3D printed concrete. *Materials* **2020**, *13*, 4919. [[CrossRef](#)]
53. Şahin, H.G.; Mardani-Aghabaglou, A. Assessment of materials, design parameters and some properties of 3D printing concrete mixtures; a state-of-the-art review. *Constr. Build. Mater.* **2022**, *316*, 125865. [[CrossRef](#)]
54. GB/T 50081-2002; Standard for Test Method of Mechanical Properties on Ordinary Concrete. Ministry of Construction of the People's Republic of China: Beijing, China, 2003.
55. GB 50010-2010; Code for Design of Concrete Structures. Ministry of Housing and Urban-Rural Development of the People's Republic of China: Beijing, China, 2011.
56. GB/T 50082-2009; Standard for Test Methods of Long-Term Performance and Durability of Ordinary Concrete. Ministry of Housing and Urban-Rural Development of the People's Republic of China: Beijing, China, 2010.

- 
57. Luo, Y.; Zheng, H.; Zhang, H.; Liu, Y. Fatigue reliability evaluation of aging prestressed concrete bridge accounting for stochastic traffic loading and resistance degradation. *Adv. Struct. Eng.* **2021**, *24*, 3021–3029. [[CrossRef](#)]
  58. Wang, B.; Yao, X.; Yang, M.; Zhang, R.; Huang, J.; Wang, X.; Dong, Z.; Zhao, H.J.M. Mechanical Performance of 3D Printed Concrete in Steam Curing Conditions. *Materials* **2022**, *15*, 2864. [[CrossRef](#)] [[PubMed](#)]

**Disclaimer/Publisher’s Note:** The statements, opinions and data contained in all publications are solely those of the individual author(s) and contributor(s) and not of MDPI and/or the editor(s). MDPI and/or the editor(s) disclaim responsibility for any injury to people or property resulting from any ideas, methods, instructions or products referred to in the content.